Mid Lift-to-Drag Ratio Rigid Vehicle 6-DoF Performance for Human Mars Entry, Descent, and Landing: A Fractional Polynomial Powered Descent Guidance Approach

Breanna J. Johnson[1] and Ronald R. Sostaric[2]
NASA Johnson Space Center, Houston, TX, 77058

Ping Lu[3]
San Diego State University, San Diego, CA 92182

Defining a feasible vehicle design and mission architecture capable of reliably delivering a payload of 20 metric tons (mt) or more is a great challenge for landing humans on Mars. The Mid Lift-to-Drag Rigid Vehicle (MRV), a rigid decelerator studied in NASA's Entry, Descent, and Landing Architecture Study (EDLAS), has shown to be a viable vehicle candidate for future human Mars missions. As the vehicle concept matures, models of increasing fidelity are added to the six-degree-of-freedom (6DoF) EDL simulation. This paper presents 6DoF simulation results using model updates for vehicle mass properties, fineness ratio, and aerodynamic-propulsive interactions. Additionally, an assessment of the Fractional-Polynomial Powered Descent Guidance (FP^{2}DG) performance is presented, and the vehicle performance is compared with the Tunable Apollo Powered Descent Guidance (TAPDG). Finally, Monte Carlo results of the vehicle design trades are presented.

I. Introduction

THE agency-wide Entry, Descent, and Landing Architecture Study (EDLAS) has been helping NASA identify the most feasible technology paths and high-payoff investments to develop human scale Entry, Descent, and Landing (EDL) systems for Mars missions. These systems would need to deliver a 20 metric ton (mt) payload or larger to the Mars surface within 50 m of the target. This study considers the Mid Lift-to-Drag ratio Rigid Vehicle (MRV), which is the rigid aeroshell vehicle that provides a feasible path to a successful human Mars mission. Enclosed rigid decelerators, like the MRV, offer protection from the harsh atmospheric and exo-atmospheric environments and reduce technology development cost and risk using flight-proven manufacturing and testing methods. However, managing mass and delivering payload with precision landing capability remain a challenge.

Over the past four years, the Entry, Descent and Landing Architecture Study (EDLAS) has continued to mature the MRV vehicle design [1, 2, 3, 4]. As the vehicle design matures, new models are implemented into simulations to determine the impact to EDL performance parameters like miss distance, peak heating, peak g-loads, and propulsion. This paper summarizes model updates made during EDLAS Phase 3 which include vehicle mass properties (Section II) and aerodynamic-propulsive interactions in Section II.B [5]. This paper also explores how trajectory performance sensitivities to changes in payload mass and vehicle length in Section II.C. Additionally, significant improvements in propellant usage and targeting have been shown in 3-Degree-of-Freedom (3-DoF) trajectory studies with the implementation of the Augmented Apollo Powered Descent Guidance (A^{2}PDG) and the Fractional Polynomial Powered Descent Guidance (FP^{2}DG) laws [2, 6]. Therefore, this paper also describes how the different powered descent guidance laws affect 6-DoF EDL performance in nominal and as off-nominal dispersed cases in Section II.A. A trade study is presented to optimize the set of gains to decrease propellant usage without sacrificing in robustness. Any savings in propellant usage are considered very valuable in vehicle and mission design, as they would reduce overall vehicle mass at launch and lower cost estimates for future missions.

---

[1] Aerospace Engineer, Flight Mechanics and Trajectory Design Branch NASA JSC/EG5.
[2] Aerospace Engineer, Flight Mechanics and Trajectory Design Branch NASA JSC/EG5.
[3] Professor and Chair, Department of Aerospace Engineering; plu@sdsu.edu, Fellow AIAA.

II. Model Update Effects on Trajectory Performance

The Flight Analysis and Simulation Tool (FAST) is used to model 6-DoF dynamics for each suggested update. For entry, the MRV uses the Fully Numerical Predictor-corrector Entry Guidance (FNPEG) which departs from traditional bank angle entry guidance algorithms, as each bank angle command is found through an iterative prediction-correction process each guidance cycle. This method is in contrast to the table lookup methods used in heritage Apollo entry guidance due to its strengthened ability to correct for Entry Interface (EI) dispersions and aerodynamic uncertainties during flight [7]. The MRV control system includes two aerosurfaces, serving as a combined elevon and rudder, and a reaction control system (RCS) comprised of twenty 4,448 N (1,000 lbf) and eight 2,224 N (500 lbf) jets. These RCS jets are also used in conjunction with the eight 100 kN main engines (MEs) for descent and landing operations. The locations of these jets are shown in Fig. 1. For descent and landing, the MRV has been using Tunable Apollo Powered Descent Guidance (TAPDG). The integrated end-to-end performance of this law is shown in Ref. 3 and serves as the basis of comparison for the trade studies discussed in this paper.

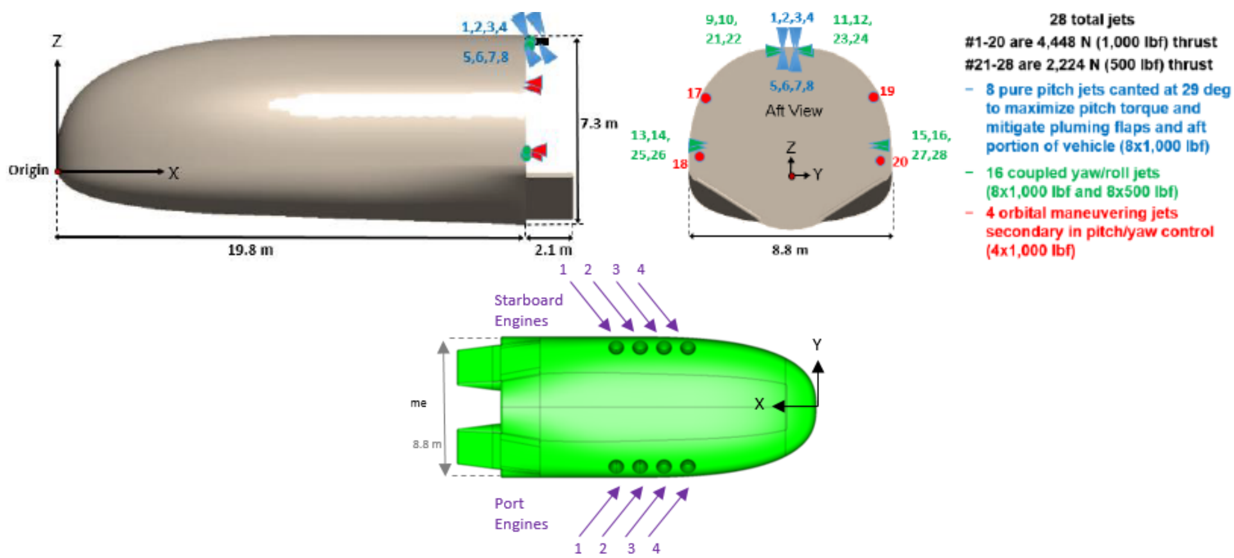

Fig. 1 Mid L/D Rigid Vehicle RCS and main engine locations.

The vehicle's Outer Mold Line (OML) was generated by the Co-Optimization Bluntbody Re-entry Analysis (COBRA) tool, which optimizes aerodynamic and aerothermal properties to inform Thermal Protection System (TPS) mass estimates [8, 9]. Recent structural analysis has led to a decrease in overall vehicle mass, changing the estimated mass at EI from 61.8 mt to 58.8 mt. The new design aligns the center of gravity (CG) of the MRV with the intended launch vehicle, the Space Launch System (SLS), by shifting the Z_{CG} from 1.0 m to 0.55 m. To accommodate the shift in Z_{CG}, a corresponding shift in target X_{CG} was made to maintain aerodynamic trim characteristics. New trajectory results shown in this paper incorporate this shift and start at an EI of 125 km altitude and velocity of 4.7 km/s. The EI velocity points North and has a relative flight path angle of -10.2 deg. The atmosphere is modeled using Mars Global Reference Atmospheric Model (GRAM) 2010 and the gravity is modeled by a Lagrangian 85x85 gravitational field. Entry guidance is run at 1 Hz, while entry controls logic is updated at 25 Hz. Descent and landing guidance is also currently run at 40 Hz, although 3-DoF results indicate that this may be reduced to 10 Hz [2]. As shown in Fig. 2a, the shift in Z_{CG} has not significantly affected the longitudinal or lateral directional stability of the vehicle, since we are able to maintain the same desired trim angle of attack of 55 deg and sideslip angle of 0 deg. However, it should be noted that this change has decreased the nominal elevon deflection profile shown in Fig. 2b, reducing the range of CG dispersions that the elevon can protect against without Reaction Control System assistance. Positive elevon deflections produce negative pitching moments, so the decrease in nominal elevon deflection angle increases protection against uncertainties in CG closer towards the aft and decreases protection closer towards the nose. It is also noted that flap deflection rate limits of 10 deg/s are imposed and simulated based on preliminary mechanical analysis for feasible large scale aerosurface mechanisms [3]. These mass property updates form the new baseline vehicle design is used throughout the analysis.

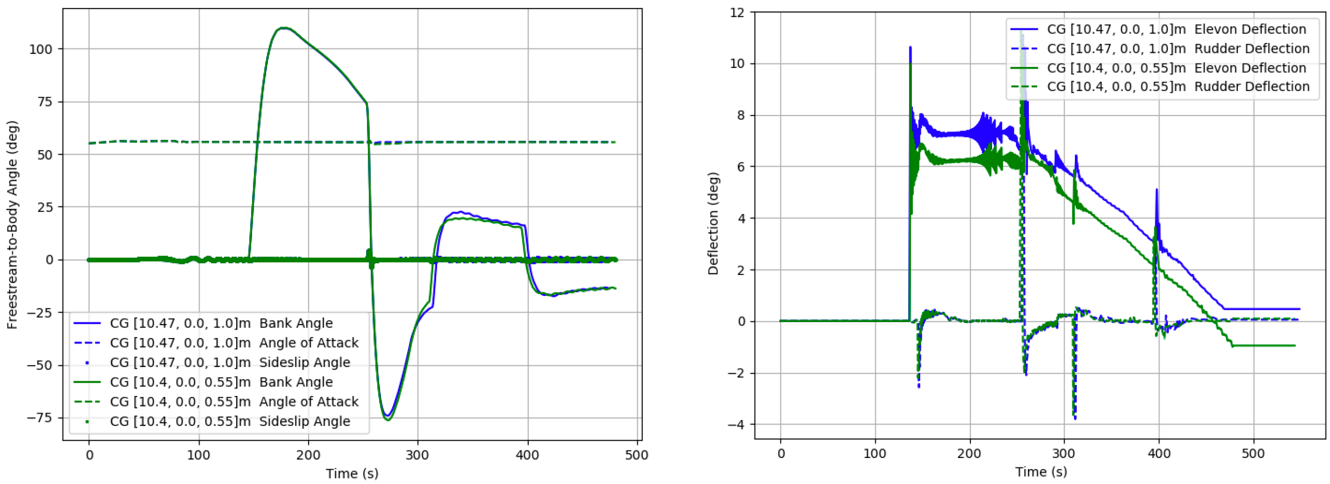

(a) (b)

Fig. 2 Mass property update effects on trajectory performance: a) Entry attitude; b) Aerosurface deflection.

A. Guidance and Control Updates

The recently developed guidance laws of A^2PDG and FP^2DG have been incorporated into the 6-DoF trajectory simulation to determine how much they improve the performance parameters of propellant usage, miss distance, and touchdown velocity. While both guidances have been demonstrated with impressive results in 3-DoF [2, 6], it is noted that modeling with the increased fidelity of 6-DoF simulations can provide an estimate of true performance by incorporating the physical limitations of the modeled control systems. For descent and landing, the MRV utilizes the RCS to provide attitude control and the eight 100 kN main engines to track throttle commands and provide stability in the presence of CG uncertainties.

TAPDG has been used in previous 6-DoF studies to reach the desired 12.5 m altitude above the landing site [3]. From this altitude, the vehicle performs a constant velocity vertical descent at 2.5 m/s. This phase improves estimated state inputs to guidance and increases the accuracy of the autonomous landing and hazard avoidance technology that may be employed on future missions. While navigation algorithms and their applications are not covered in this paper, including the vertical descent phase and assessing the performance of this phase determines which guidance gains would lead to better integrated guidance, navigation, and control (GN&C) performance. One motivation to upgrade the descent guidance from TAPDG to FP^2DG stems from the dependence on a user-defined time-to-go (t_{go}). This t_{go} defines the time to go until the tunable Apollo guidance law ends, but there is neither an intuitive nor optimal way to choose the initial value of t_{go} and where to begin powered descent. This powered descent initiation (PDI) point is typically chosen through trial and error and is associated with a user-defined range-to-go. The PDI point is critical in reducing propellant usage and providing sufficient margin for dispersed cases, but the most optimal PDI is case dependent.

To achieve Monte Carlo simulation results where all cases land within 50 m of the target [3], the tunable Apollo law was augmented with the quartic t_{go} equation from Ref. 10. The solution to this equation would estimate the appropriate t_{go} given the user-defined range-to-go. This equation is defined by

$$t_{go}^4 + \frac{-2\left[\boldsymbol{V}^T\boldsymbol{V}+\boldsymbol{V}_f^T(\boldsymbol{V}+\boldsymbol{V}_f)\right]}{\left(\Gamma+\frac{\boldsymbol{g}^T\boldsymbol{g}}{2}\right)} t_{go}^2 + \frac{-12\left(\boldsymbol{r}-\boldsymbol{r}_f\right)^T\left(\boldsymbol{V}+\boldsymbol{V}_f\right)}{\left(\Gamma+\frac{\boldsymbol{g}^T\boldsymbol{g}}{2}\right)} t_{go} + \frac{-18\left(\boldsymbol{r}-\boldsymbol{r}_f\right)^T\left(\boldsymbol{r}-\boldsymbol{r}_f\right)}{\left(\Gamma+\frac{\boldsymbol{g}^T\boldsymbol{g}}{2}\right)} = 0 \tag{1}$$

where Γ is a user provided weighting factor, V is the planet relative velocity, r is the planetocentric position, g is the planet gravity, and the subscript f indicates the target final velocity and position. However, the range-to-go was not optimized and was chosen by trial and error. In contrast, FP^2DG automatically determines the optimal time for PDI without a pre-defined t_{go} or range-to-go input [2, 6]. FP^2DG uses an internal Universal Powered Guidance (UPG) algorithm to predict the PDI point by solving the fuel-optimal soft-landing problem [11]. The FP^2DG guidance law also allows for better control over shaping the descent trajectory profiles by allowing the user to adjust the gains of k_r and γ in the thrust acceleration command, $\boldsymbol{a_T}$, as defined by

$$\boldsymbol{a_T} = \gamma\left[\frac{k_r}{2(\gamma+2)} - 1\right]\boldsymbol{a_{T_f}} + \left[\frac{\gamma k_r}{2(\gamma+2)} - \gamma - 1\right]\boldsymbol{g} + \frac{\gamma+1}{t_{go}}\left(1 - \frac{k_r}{\gamma+2}\right)\left(\boldsymbol{V_f} - \boldsymbol{V}(t)\right) + \frac{k_r}{t_{go}^2}\left(\boldsymbol{r_f} - \boldsymbol{r} - \boldsymbol{V}(t)t_{go}\right) \tag{2}$$

If a gain of $\gamma = 1$ is chosen in Equation 2, we arrive at the A^{2}PDG law from Ref. 2.

$$\boldsymbol{a_T} = \frac{2}{t_{go}}\left(1 - \frac{1}{3}k_r\right)\left[\boldsymbol{V_f} - \boldsymbol{V}(t)\right] + \frac{k_r}{t_{go}^2}\left[\boldsymbol{r_f} - \boldsymbol{r}(t) - \boldsymbol{V}(t)t_{go}\right] + \frac{1}{6}(k_r - 6)\boldsymbol{a_{T_f}} + \frac{\mathbf{1}}{\mathbf{6}}(k_r - 12)\boldsymbol{g} \tag{3}$$

As suggested in Ref. 6, Equation 2 represents families of explicit guidance laws for any value of $k_r \geq 2(\gamma + 2)$. Note that Equation 3 shows the same tunable Apollo guidance law used in past 6-DoF MRV studies [3].

The similarities between TAPDG and FP^{2}DG are evident, but FP^{2}DG contains an additional gamma term for even finer trajectory shaping. In order to find the best gain set for minimal propellant usage, miss distance, and final velocity, a trade study on γ and k_r was performed for nominal trajectories. It is noted that an update to the controls model has been implemented to increase the minimum delta throttle achievable by the main engines from a conservative 2,000 N to 100 N, leading to smoother throttle profiles and better throttle tracking. However, this update had no significant impact on performance. Conversely, the UPG provided PDI point did have a significant impact on performance. When comparing the nominal trajectory profiles from TAPDG and FP^{2}DG for the same gains of $k_r = 9.0$ and γ=1, we see in Fig. 3 that the PDI for the TAPDG profile begins earlier and ends later than FP^{2}DG, leading to higher propellant usage. And although the pitch and position profiles are very similar, the throttle profiles are very different. Following the main engine startup and CG balancing phases, the TAPDG trajectory follows a roughly linear profile, while FP^{2}DG follows a more agile parabolic profile before concluding with the constant velocity vertical descent (12.5 m altitude) and main engine cutoff sequence (1 m altitude). All plots in Fig. 3 show only the powered descent phase of flight. The later PDI of FP^{2}DG allows for a reduction in propellant usage by an order of 1 mt! This is an impressive reduction on the order of ~2 % of the vehicle mass at EI.

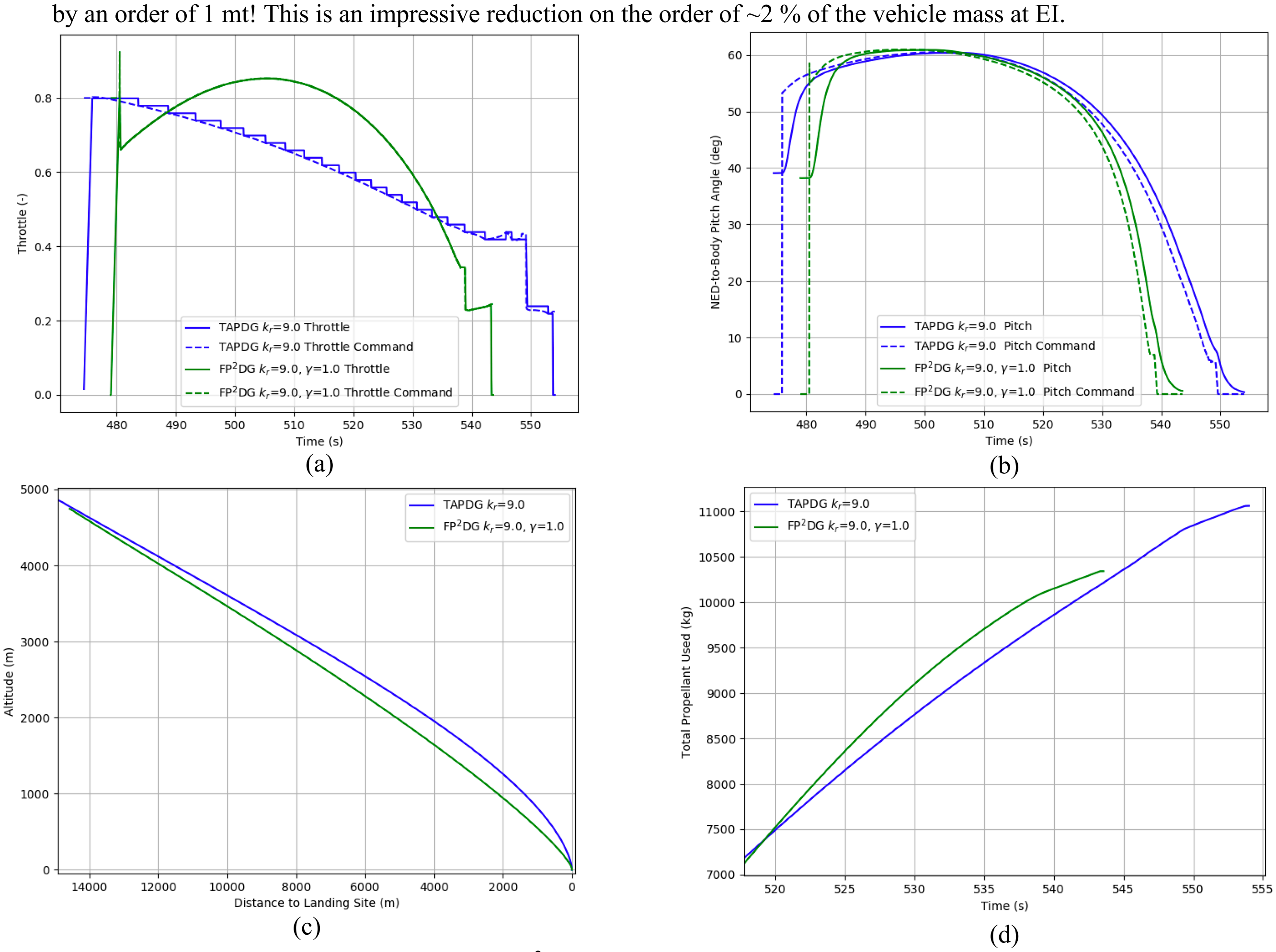

Fig. 3 Comparison of TAPDG and FP^{2}DG: a) Throttle; b) Pitch; c) Position; d) Propellant usage.

An innate feature of FP²DG is the flexibility to explore new families of the explicit tracking laws from which A²PDG and TAPDG are derived. Previous 3-DoF studies have shown that the most propellant optimal form of A²PDG arises when selecting a gain of $k_r = 6$, which is the same as the E-guidance law [2, 6]. The E-guidance law, which is a solution to an optimal landing problem in a constant gravity field, was developed during the Apollo era as a possible alternative to Apollo guidance, but it was never flown. In previous 6-DoF trades, this gain choice was determined to be too marginal in dispersed cases due to the large pitch angles commanded at the end of TAPDG and beginning of the vertical descent phase. For 3-DoF FP²DG cases, it was found that smaller values of γ can lead to smaller pitch angles at the end of powered descent [6]. Using the k_r and γ relation $k_r \geq 2(\gamma + 2)$ for the guidance law in Equation 2, Fig. 4 explores other minimum k_r gains for fractional values of γ. All plots in Fig. 4 show powered descent with FP²DG until a time of ~538 s, followed by the gravity turn constant vertical descent phase. As expected, Fig. 4a shows that decreasing values of γ does result in decreased final FP²DG pitch angles, but these changes are very small. All cases still struggle to follow the sharp change in pitch command due to limited pitch control authority and thus incur undesirable increases to the flight path angle (-90 deg implies pure vertical velocity). Figures 4c-d show that the vertical velocity of 2.5 m/s is maintained before main engine shutoff, but the total relative velocity increases sharply due to residual horizontal velocity (in the North-East direction) incurred by limited control system authority to follow the sharp change in pitch at the guidance transition point.

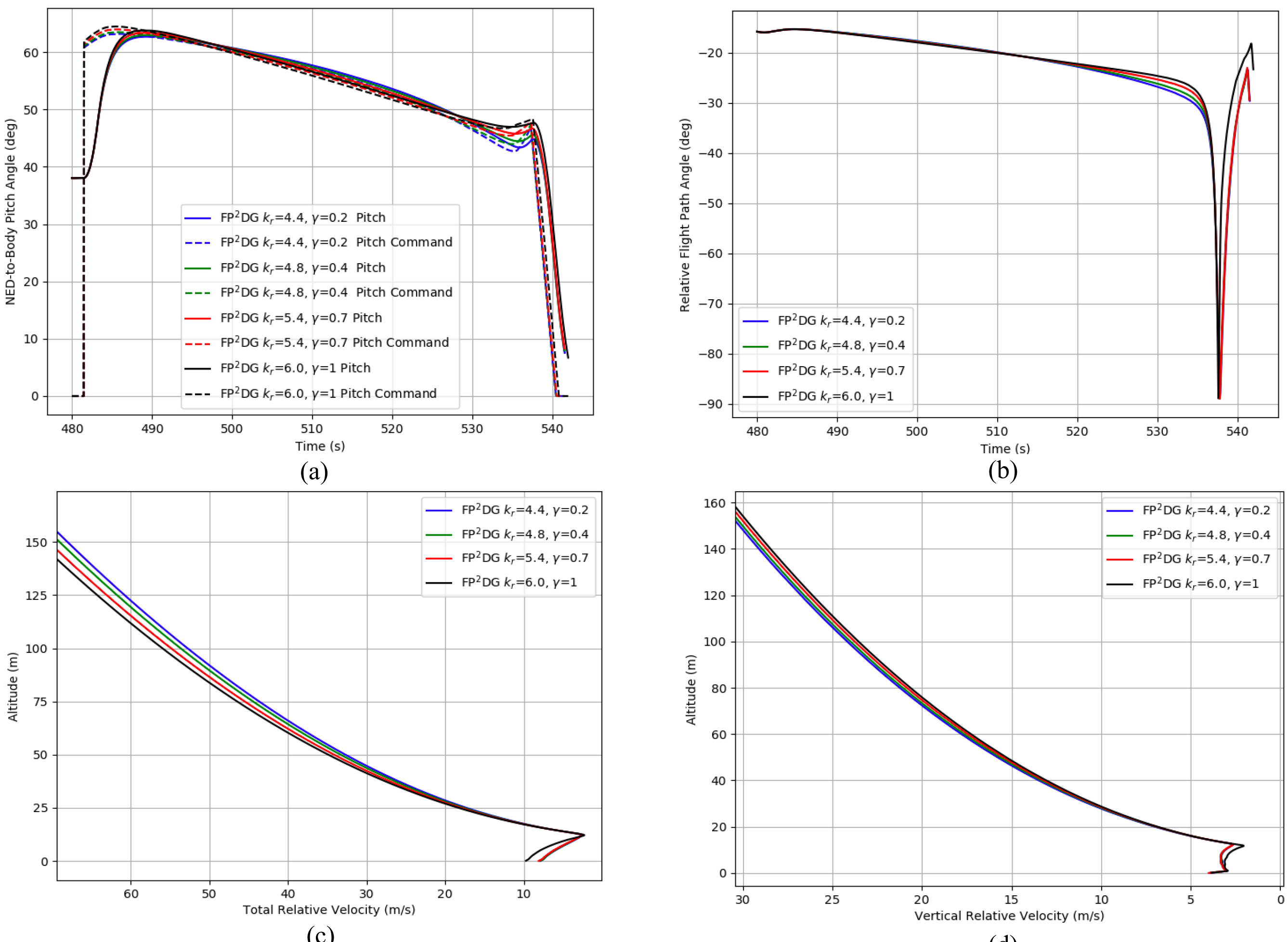

Fig. 4 Minimum values of k_r for different values of γ: a) Pitch; b) Relative flight path angle; c) Energy; d) Energy profile (vertical).

From this study, it became clear that 6-DoF trajectories would need gains of k_r larger than the minimums found from the k_r and γ relation. In fact, small increases to k_r above the minimum resulted in significantly different trajectory profiles as evidenced by the parabolic throttle curves shown in Fig. 5a, the smaller pitch angles at FP²DG termination shown in Fig. 5b, and the reduced horizontal velocities at the ground shown in Figs. 5c-d. These improvements are due to the smoother handover between the FP^{2}DG and gravity turn attitude commands. It is difficult to have a perfectly vertical velocity gravity turn, where all of the velocity is directed in the nadir direction, due to the fact that the control system has only a few seconds to correct errors in the pitch channel, and any large errors can significantly negatively impact final velocity and miss distance at the ground. Future analysis should be completed to determine how much the use of main engines for attitude control can help this problem, since the pitch authority of these engines is much greater than that of the RCS.

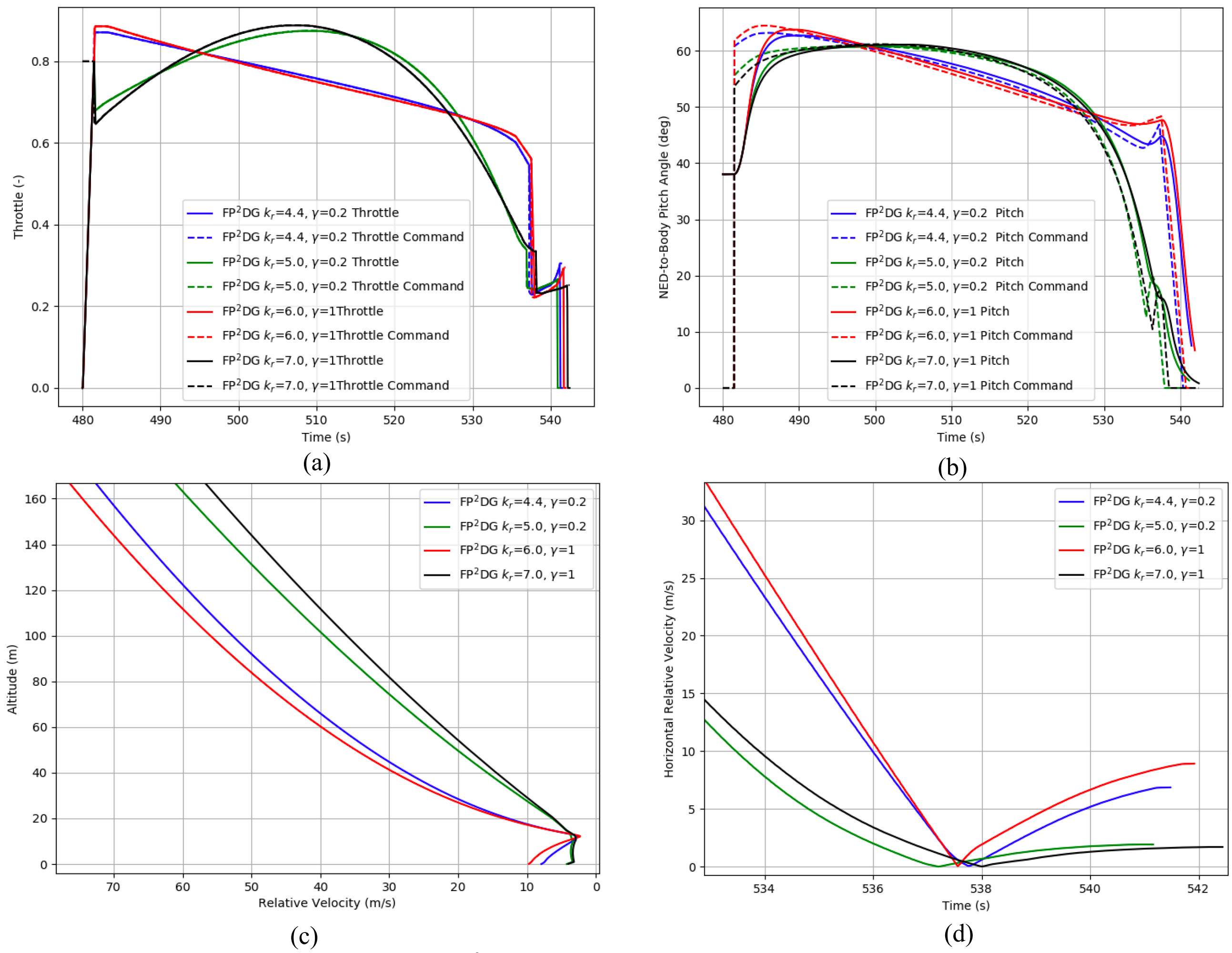

Fig. 5 Performance comparison of FP^{2}DG gains: a) Throttle; b) Pitch; c) Energy; d) North-East velocity.

Since the pitch profile improvements of using γ values of less than 1 were small, other trade studies on nominal trajectories in this paper will use a $\gamma = 1$. Again, this gain results in the same tunable law common to both TAPDG and A^{2}PDG. When this trade was done for the heritage Apollo guidance law, where $\gamma = 1$ and $k_r = 12$, similar performance to the $\gamma = 1$ and $k_r = 7$ case shown in Fig 5 was found. There was a small increase in propellant and small decrease in final pitch angle, but the change in performance was less significant than what is shown in Fig 5. The best gain set will be determined by Monte Carlo analysis in Section III.

B. Aerodynamic Environment Updates

Until EDLAS conducted higher fidelity vehicle analysis in Phase 3, the trajectory simulation assumed that, after descent engine initiation, thrust was the dominant force on the vehicle, and therefore, all aerodynamic forces and moments on the vehicle were set equal to zero during this phase of flight. However, for large human-scale landers like the MRV, where the nozzles are scarfed and canted outboard 10 deg along the edge of the vehicle forebody, the vehicle has a large aerodynamic surface area unobstructed by the engine plumes. In fact, depending on the engine configuration, aerodynamic axial force equivalent to the thrust of a single engine or more can be produced after PDI as the vehicle decelerates from supersonic to transonic speeds [5]. Aerodynamic-propulsive interference models are complex and computationally expensive to run. The preliminary model included here utilizes results from the OVERset gridFLOW solver (OVERFLOW) [12]. OVERFLOW is run for both the powered and unpowered vehicle configuration at several powered descent flight Mach numbers. The difference between the axial force coefficients of the powered and unpowered results provide the basis for the model. However, the aerodynamic-propulsion model assumes the vehicle uses 120 kN main engines at a constant 80% throttle (96 kN) and constant angle of attack (90 deg) [5]. As shown in the TAPDG angle of attack profiles in Fig. 6a, these assumptions differ from the guidance and control (G&C) profiles studied in this paper. Results in Fig. 6b show the dynamic pressures during powered descent. Further work remains to accurately model the powered descent phase with an aerodynamic-propulsive database using different angles of attack and throttle levels. Additionally, the database will also include results from other tools like Data-Parallel Line Relaxation (DPLR) to provide validation [13].

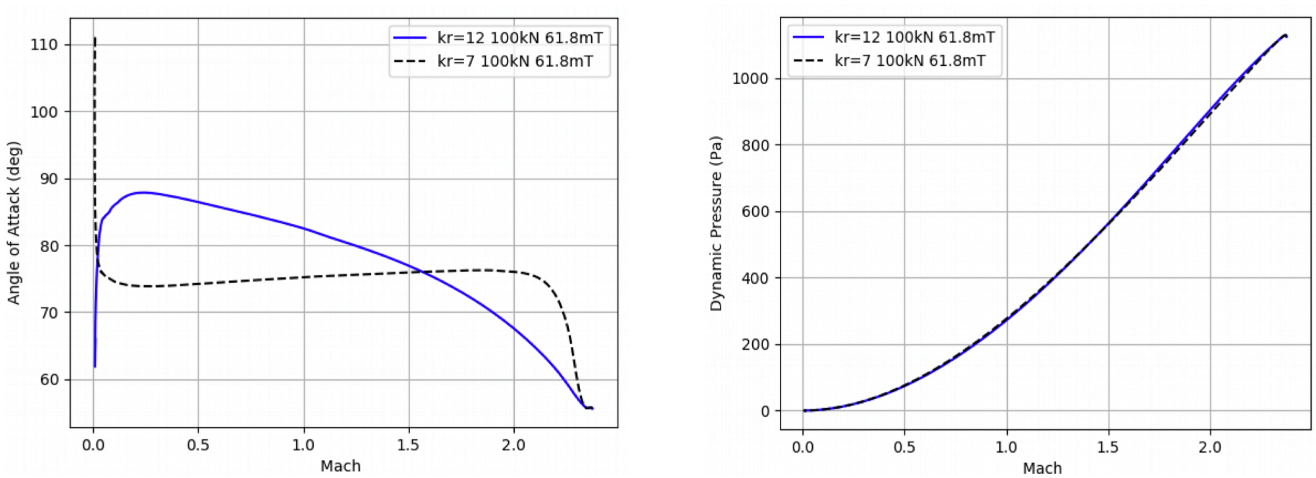

(a) (b)

Fig. 6 TAPDG profiles for different values of k_r: a) Angle of attack; b) Dynamic pressure.

Although the assumptions used to generate the aerodynamic-propulsion interaction model do not characterize the non-constant throttle and non-constant angle of attack profiles, the preliminary model is applied to the nominal case to help gain insights into how the interaction effects change current vehicle and G&C assumptions.

The MRV descent trajectories have four segments: main engine startup, CG balancing, powered descent guidance law tracking, and vertical descent. Figure 7 shows that when an aerodynamic-propulsive interaction model is included, the time spent in the CG balancing phase increases. The conclusion of this balancing phase is illustrated in Fig. 7f whenever the ME pitch command first becomes non-zero, indicating that FP^{2}DG pitch commands may be followed once stability is achieved. One way to mitigate the CG balancing is to change the distance between the engines. Since there are no current packaging constraints on main location, a trade study was performed to determine a control optimal space between engines along the X-axis only. The results are shown in Fig. 7. ME Δx denotes the additional displacement distance between engines and ranges from 0 m to 1.5 m. The current main engine configuration is able to produce a collective maximum pitch torque of roughly 350,000 Nm, but initial studies suggest that this can be increased to 600,000 Nm or more if the distance between each engine is increased. The CG balancing phase typically only takes a couple of seconds, even in dispersed cases with CG offsets. However, the aerodynamic pitch moments introduced are significant, as evidenced by the large negative moments shown in Fig. 7a and the saturation of the main engines at their collective maximum pitch authority as shown in Fig. 7b. Once stability is reached, the main engine maintains a constant positive pitching moment to counteract any persistent biases to the system.

In addition to expanding the aerodynamic-propulsion interaction model to include MRV vehicle configurations with different throttle settings and engine spacing, considering trim angles of attack trim point below 90 deg is significantly important to include in future interaction models. A pitch up maneuver to the expected new trim point of ~80 deg is included in the plots of Fig.7 prior to starting the main engines to help decrease the magnitude of aerodynamic pitch moment on the system for future studies. It is shown that the stronger the pitch control authority, the faster the vehicle is able to resume close tracking of the given pitch commands from guidance as shown in Figs. 7b and 7c. Figure 7d shows that after the CG balancing phase, cases with increased distances between main engines result in smoother throttle profiles. This is due to the fact that the guidance must compensate for the time spent stabilizing the vehicle. Figure 7e shows the position profiles for each case, demonstrating the ability to land within 5 meters of the target, similar to the case without the aerodynamic-propulsion interaction modeled (blue line).

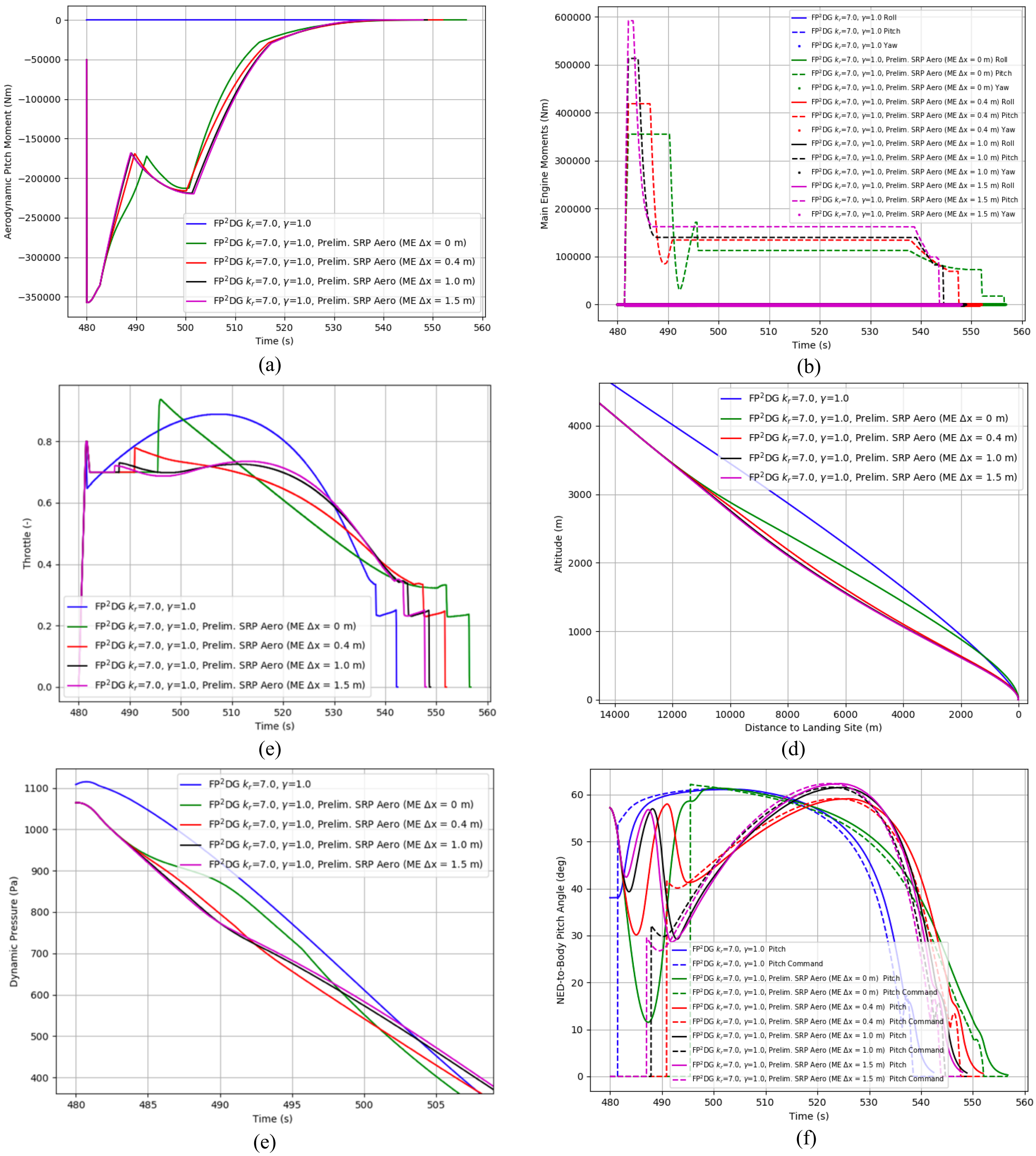

Fig. 7: Effects of preliminary SRP aerodynamics on trajectory profiles: a) Aerodynamic pitch moment; b) Main engine pitch moment; c) Throttle; d) Position; e) Dynamic pressure; f) Pitch.

Due to the differences in the assumptions used to create the preliminary aerodynamic interaction model, Monte Carlo analysis of the engine spacing trade is future work. However, the results of this trade study give important insights into new challenges. If the large pitching moment persists across all angles of attack, mitigation strategies to improve performance include increasing the thrust of the RCS pitch jets, introducing a dynamic pressure trigger for PDI, and increasing the space between the main engines along the X-axis, which remains the primary mitigation strategy. These results show that tracking performance does indeed improve for increased values of ME Δx.

C. Concept of Operations and Vehicle Trades

Changes to a vehicle's payload mass and shape can have many subsystem impacts. Most notably, increases to payload mass can change the amount of TPS needed to withstand the high heating associated with entry. Therefore, a TPS sizing study was performed using the TPSSizer tool for the MRV with a 20 mt vs. a 22 mt payload [4, 14]. Mass estimation relationships were used to iteratively size other subsystem components to achieve an integrated and closed vehicle design. Lastly, the COBRA tool was used with TPSSizer to perform a fineness ratio (FR) study, where FR is the ratio of the vehicle length to diameter, to examine MRV scalability. The current baseline, which has an FR = 2.25, can be reduced to an FR = 1.78 to fit inside the 10 m short payload fairing (PLF) of the SLS Block II configuration [4]. The current vehicle assumes use the 10 m long PLF. An update in FR corresponds to a change in the length of the vehicle, shortening it from 19.8 m to 15.7 m as shown in Fig. 8. This change in FR resulted in updates to aerodynamic force and moment calculations, the modeled CG, and the overall system mass. To maintain similar aerodynamic characteristics and agreement with the SLS CG requirements, the targeted CG location for the scaled vehicle is [8.27, 0, 0.55] m. Although there was a small increase in estimated TPS mass, reduction in length and area led to a mass reduction of ~4 mt and an EI arrival mass of 54.9 mt. It should be noted that future work will include re-running the Cart3D tool to fully capture any changes in the aerodynamics that are not captured with simply applying scaling factors. For the purposes of the work presented in this paper, the Cart3D aerodynamic coefficients generated for the FR=2.25 baseline model are scaled for the FR=1.78 model to indicate the likely trajectory performance impacts of a shorter MRV.

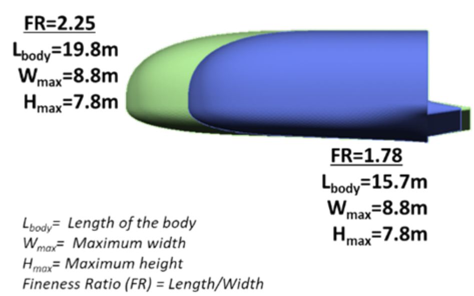

Fig. 8 Comparison of Fineness Ratios for the MRV.

Remarkably, due to the agile nature of the entry and powered descent G&C methods used, the significant changes to the vehicle resulted in no changes to G&C gain tuning and no large deviations in performance. Results from the TPSSizer tool suggest that PDI should begin at a lower altitude and higher velocity for the shorter vehicle. The results in Fig. 9b agree with this assumption, and Fig. 9c shows the predicted increase in heating. As expected, all trajectories maintain nearly identical bank, angle of attack, and sideslip profiles, as shown in Fig. 9a. Figure 9d shows that the smallest mass vehicle with an FR = 1.78 reaches PDI earlier and performs powered descent for a smaller amount of time as compared to the other trajectories. However, the shape of the throttle profiles between all the trajectories are nearly identical. Propellant usage follows the trend of the EI masses for each vehicle, with the lightest vehicle (shown in blue) at 54.9 mt consuming the least and the heaviest vehicle (shown in red) at 62.1 mt consuming the most. For the results in the rest of this paper, we will continue to use an FR = 2.25 and a payload of 20 mt unless the mission concepts of operations officially changes the payload mass or PLF for all candidate vehicles in the study. More information about the inputs to this trade study may be found in Ref. 4.

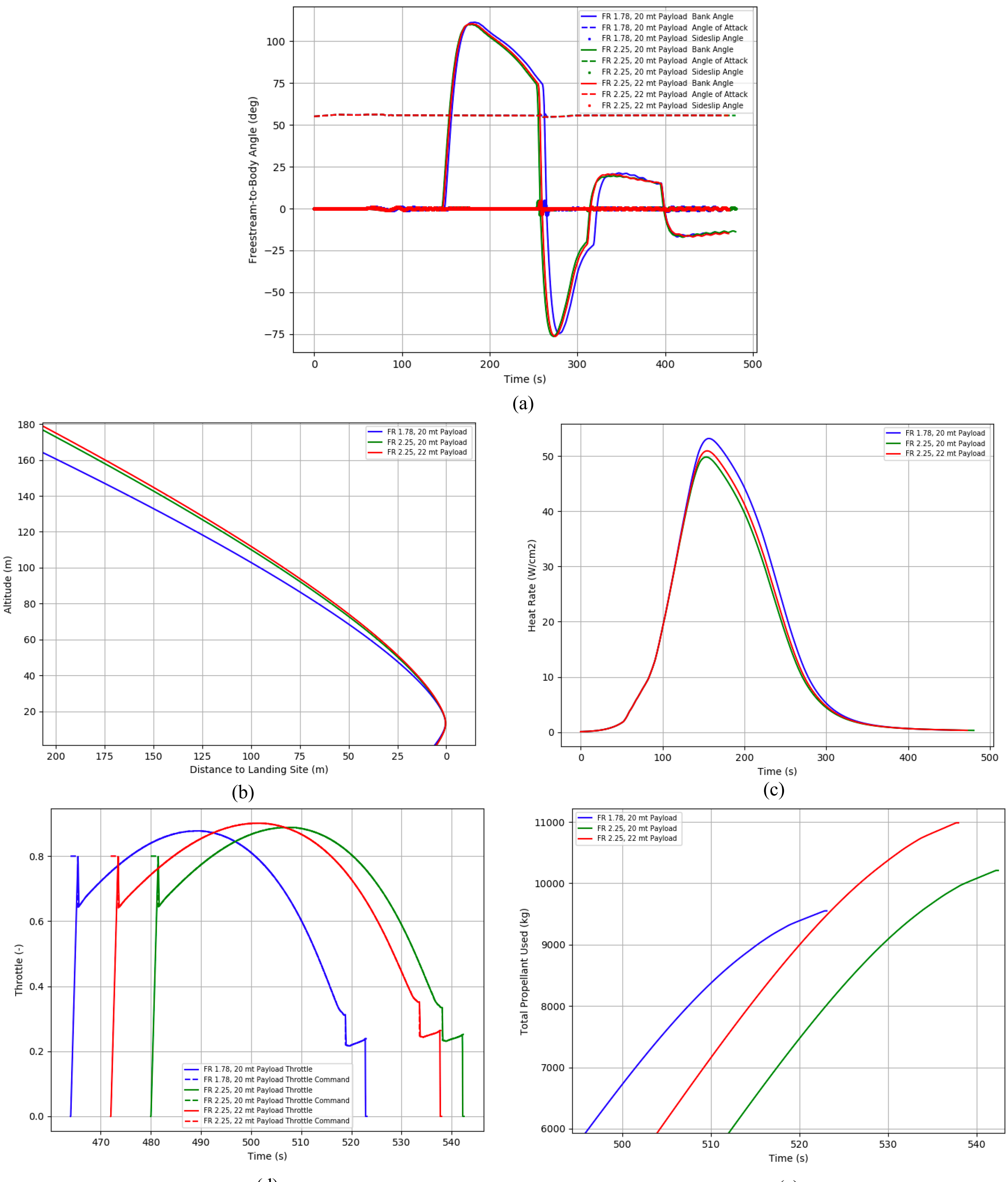

Fig. 9 Concept of operations effects on trajectory profiles: a) Attitude; b) Position; c) Heating; d) Throttle; e) Propellant usage.

III. Monte Carlo Results

This section details the results of the Monte Carlo analysis performed for the trade studies detailed in Section II. First gain sets of γ and k_r will be evaluated based on which values perform best under entry aerodynamic dispersions (C_A, C_Y, C_N, C_l, C_m, C_n), mass and inertia uncertainties, CG uncertainties, Mars GRAM atmospheric and dust tau dispersions, main engine transients and throttle dispersions, main engine lags, and entry interface dispersions such as velocity, azimuth, flight path angle, latitude, and longitude. For the results in this section, no SRP aerodynamics or uncertainties are applied until more aerodynamic database points are provided in thrust and angle of attack. Each trajectory begins at the EI conditions specified in Section II of this paper. For entry, the vehicle should stay within expected heat rate margins of 50-60 W/cm^2 and abide by the human safety requirement of no more than 4 g's for a deconditioned crew [3, 15]. It should be noted that this simulation uses the simple Chapman aerothermal equation to calculate heat rate and would differ from the higher fidelity TPSSizer heat rate calculations in magnitude [4, 15]. However, general trends in response to trajectory inputs would not change between the two simulations, and a scaling factor may be applied in post-analysis to provide closer agreement if desired.

The results of these Monte Carlos are to be compared to the current baseline, which uses TAPDG for guidance. For descent, each main engine is modeled individually with its own unique dispersions. Changes in Isp as a function of thrust are also modeled. Modeled engine limitations include descent throttle rates (80 %/s), main engine startup transients (55 %/s), minimum throttle limits (20%), and main engine shutdown transients (200 %/s). All EDL dispersions applied throughout the trajectory are shown in Tables 1-2.

Table 1. Entry Interface dispersions.

Monte Carlo Varied Parameter	Distribution	3σ / maximum	-3σ / minimum
Altitude (km)	Gaussian	1.00E-01	-1.00E-01
Longitude (deg)	Gaussian	2.50E-01	-2.50E-01
Latitude (deg)	Gaussian	2.50E-01	-2.50E-01
Velocity (m/s)	Gaussian	3.30E+00	-3.30E+00
Flight Path Angle (deg)	Gaussian	1.00E-01	-1.00E-01
Azimuth (deg)	Gaussian	1.70E-01	-1.70E-01
Mass (kg)	Gaussian	2.00E+02	-2.00E+02
Inertia (%)	Gaussian	1.00E+00	-1.00E+00
ΔX_{cg} (cm)	Uniform	2.00E+01	-2.00E+01
ΔY_{cg} (cm)	Uniform	5.00E+00	-5.00E+00
ΔZ_{cg} (cm)	Uniform	2.00E+01	-2.00E+01
CA, CN (%)	Uniform	1.00E+01	-1.00E+01
CY, Cll, Cm, Cln (deg)	Uniform	3.00E+00	-3.00E+00
Atmospheric density	Mars GRAM 2010	Mars GRAM 2010	Mars GRAM 2010
Mars GRAM 2010 dust opacity	Uniform	0.9	0.1

Table 2. Main engines 1-8 dispersions.

Monte Carlo Varied Parameter	Distribution	3σ / maximum	-3σ / minimum
ME Max Thrust (N)	Gaussian	1.00E+03	-1.00E+03
ME Throttle Rate (%)	Gaussian	1.00E+00	-1.00E+00
ME Max Isp (%)	Gaussian	1.00E+00	-1.00E+00
ME Startup Time (%)	Gaussian	1.00E+00	-1.00E+00
ME Startup Lag (s)	Uniform	2.50E-01	0.00E+00

Due to the lack of wind tunnel testing or available flight data for mid-L/D shapes, aerodynamic force and moment coefficient uncertainties are estimated with Equations 4-9 and applied in Monte Carlo simulations. U^m represents a multiplier applied to increase the uncertainty of the aerodynamic database, while U^a represents an additive uncertainty to the aerodynamic database.

$$C_A = C_{A,base} + C_{A,base} * U_{C_A}^m + \Delta C_{A_{Flaps}} \quad (4)$$

$$C_Y = C_{Y,base} + U_{C_Y}^a + C_{Y_{\delta_r}} \delta_r \quad (5)$$

$$C_N = C_{N,base} + C_{N,base} * U_{C_N}^m + \Delta C_{N_{Flaps}} \quad (6)$$

$$C_{l_{CG}} = \left[C_{l,MRC} + C_Y \frac{\Delta z}{L_{ref}} + C_N \frac{\Delta y}{L_{ref}} \right] + U_{C_l}^a + C_{l_{\delta_r}} \delta_r \quad (7)$$

$$C_{m_{CG}} = \left[C_{m,MRC} + C_A \frac{\Delta z}{L_{ref}} - C_N \frac{\Delta x}{L_{ref}} \right] + U_{C_m}^a + \Delta C_{m_{Flaps}} \quad (8)$$

$$C_{n_{CG}} = \left[C_{n,MRC} - C_A \frac{\Delta y}{L_{ref}} - C_Y \frac{\Delta x}{L_{ref}} \right] + U_{C_n}^a + C_{n_{\delta_r}} \delta_r \quad (9)$$

Aerodynamic coefficients that are zero at trim conditions are added with an estimated ± 3 deg uncertainty maximum delta from trim in sideslip or angle of attack. Additionally, force coefficients that are non-zero at trim conditions are added with an estimated 10% uncertainty. Thus, the uncertainty terms in Equations 4-9 are bounded by the following:

$$U_{C_A}^m = \mathrm{x} \in [-0.1, +0.1]$$

$$U_{C_Y}^a = \mathrm{x} \in [-1, +1] * U_{C_{Y,max\beta}}^a$$

$$U_{C_N}^m = \mathrm{x} \in [-0.1, +0.1]$$

$$U_{C_l}^a = \mathrm{x} \in [-1, +1] * U_{C_{l,max\beta}}^a$$

$$U_{C_m}^a = \mathrm{x} \in [-1, +1] * U_{C_{m,\max\alpha}}^a$$

$$U_{C_n}^a = \mathrm{x} \in [-1, +1] * U_{C_{n,max\beta}}^a$$

Results of wind tunnel testing would help to better inform the simulated uncertainties for the forebody and flaps.

A. Gain Tuning Trade Study Results

Results from 3,000 case Monte Carlo trades of the FP^2DG gain sets are shown in Tables 3-6. Table 3 shows the previously found results for the TAPDG case at $k_r = 9$, and Table 4 shows how these results change with FP^2DG performance. Only the performance of the descent and landing phases of flight is presented in this section since the changes of the key entry performance parameters are not significant from the TAPDG study and still abide by all constraints. As desired, parameters like average miss distance and velocity improve with the use of the predictive PDI logic in FP^2DG. The most significant change is that the new average propellant usage has decreased by more than 1 mt from the original value. In fact, the new average is better than the best 0.25% percentile (0.25%-tile) of cases using TAPDG. Additionally, the horizontal velocity has improved at the 99.75%-tile, implying improved navigation system performance would be achievable with FP^2DG. Table 5 shows a comparison of the mean statistics for each gain set, while Table 6 shows the 99.75%-tile values. Similar to the performance shown in Refs. 2 and 3, we see that each FP^2DG case is able to achieve sub-meter accuracy from the landing site and near zero horizontal velocities at 12.5 m altitude. No cases reach this point or land outside of the 50 m requirement given the listed assumptions above. However, as discussed in Section II.A, we do see that the final relative flight path angle at the vertical velocity initiation point is an indicator for landing accuracy and magnitude of residual horizontal velocities due to the limitations introduced by modeling the control system. If propellant usage becomes a stronger driver than miss distance or horizontal velocity, we see that a gain set of γ = 0.2 and k_r= 5 provides similar performance with smaller propellant costs. The comparison of these gains is shown in Fig. 10. Based on these results, the gain set of γ = 1 and k_r= 9 for FP^2DG will be used as the new baseline for trajectory sims due to the small horizontal velocities at the 12.5 m altitude. It should be noted that the final vertical velocities at the ground are slightly larger than the targeted 2.5 m/s due to the fact that the main engines must be shut down before impact. For Apollo lunar missions, this occurred at ~1 m above the landing site to minimize plume surface interaction and limit the damaging of the vehicle. While these results are promising, more work must be done to decrease the horizontal velocities incurred in the constant vertical velocity descent phase.

Table 3. Monte Carlo results for TAPDG at the ground (k_r = 9).

Parameter	Mean	Standard Deviation	99.75%-tile	0.25%-tile
Miss Distance (m)	4.30E+00	1.34E+00	9.26E+00	1.35E+00
Horizontal Velocity (m/s)	1.08E+00	3.21E-01	3.35E+00	6.09E-01
Vertical Velocity (m/s)	3.61E+00	6.4E-02	3.78E+00	3.47E+00
ME Propellant Used (mt)	1.13E+01	3.20E-01	1.23E+01	1.04E+01
RCS Propellant Used (mt)	5.87E-01	1.45E-01	1.03E+00	2.66E-01
Pitch Angle (deg)	3.09E-01	2.89E-01	2.02E+00	6.00E-02

Table 4. Monte Carlo results for FP^{2}DG at the ground (k_r = 9, γ = 1).

Parameter	Mean	Standard Deviation	99.75%-tile	0.25%-tile
Miss Distance (m)	2.79E+00	6.85E-01	5.72E+00	1.10E+00
Horizontal Velocity (m/s)	9.29E-01	2.68E-01	2.48E+00	4.70E-02
Vertical Velocity (m/s)	3.69 E+00	3.20E-02	3.79E+00	3.62E+00
ME Propellant Used (mt)	1.00E+01	3.77E-01	1.11E+01	8.94E+00
RCS Propellant Used (mt)	3.50E-01	7.47E-02	6.64E-01	2.18E-01
Pitch Angle (deg)	4.82E-01	2.10E-01	2.47E+00	2.78E-01

Table 5. FP^{2}DG gain comparison of Monte Carlo 99.75%-tile results at 12.5 m altitude.

Parameter	γ = 0.2, k_r= 5 **99.75%-tile**	γ = 1, k_r= 7 **99.75%-tile**	γ = 1, k_r= 9 **99.75%-tile**	γ = 1, k_r= 12 **99.75%-tile**
Miss Distance (m)	6.27E-01	7.25E-01	1.52E-01	4.58E-01
Horizontal Velocity (m/s)	6.52E-01	8.14E-01	4.62E-01	4.40E-01
Vertical Velocity (m/s)	3.36E+00	2.94E+00	2.91E+00	3.02E+00
ME Propellant Used (mt)	1.07E+01	1.08E+01	1.09E+01	1.09E+01
RCS Propellant Used (mt)	6.46E-01	6.51E-01	6.46E-01	6.61E-01
Pitch Angle (deg)	1.96E+01	1.69E+01	1.36E+01	1.10E+01
Relative Flight Path Angle (deg)	-7.75E+01	-7.08E+01	-7.96E+01	-8.45E+01

Table 6. FP^{2}DG gain comparison of Monte Carlo 99.75%-tile results at the ground.

Parameter	γ = 0.2, k_r= 5 **99.75%-tile**	γ = 1, k_r= 7 **99.75%-tile**	γ = 1, k_r= 9 **99.75%-tile**	γ = 1, k_r= 12 **99.75%-tile**
Miss Distance (m)	9.09E+00	1.34E+01	5.72E+00	6.96E+00
Horizontal Velocity (m/s)	3.83E+00	6.14E+00	2.48E+00	2.41E+00
Vertical Velocity (m/s)	4.56E+00	4.09E+00	3.79E+00	3.79E+00
ME Propellant Used (mt)	1.10E+01	1.10E+01	1.11E+01	1.11E+01
RCS Propellant Used (mt)	6.71E-01	6.75E-01	6.64E-01	6.80E-01
Pitch Angle (deg)	2.02E+00	2.35E+01	2.47E+00	2.54E+00

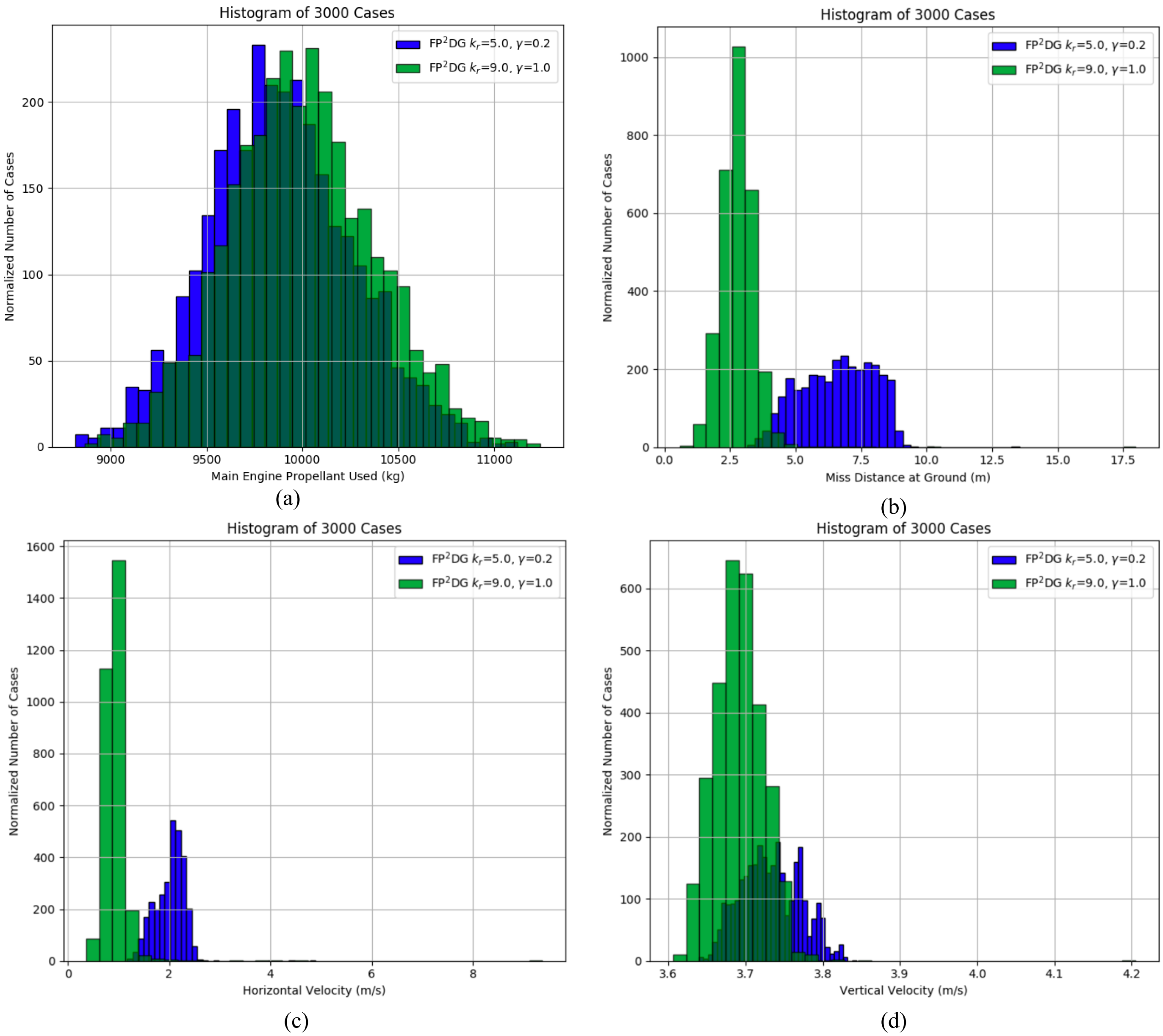

Fig. 10 Comparison of key performance parameters at the ground for gain sets (γ = 0.2, k_r= 5.0) and (γ = 1.0, k_r= 9.0) : a) Main engine propellant usage; b) Miss distance; c) North-East velocity; d) Down velocity.

B. Vehicle Modification Trade Study Results

Using the gains of γ = 1.0 and k_r= 9.0 found above in Section III.A, the results from 3,000 case Monte Carlo trades for changes to the vehicle are shown in Table 7. The Monte Carlo simulation results for all options in the trade study maintained the desired heat rates within 50-60 W/cm^2 and g-loads below 4 g's for the 99.75%-tile. As expected, all simulations complete with similar performance statistics to that of the 100 kN, 20 mt, FR = 2.25 baselined case. The trend of increased propellant usage with increased EI mass is preserved as seen in the nominal results from Section II.C. Similarly, higher peak heat rates are associated with the FR = 1.78 scaled vehicle due to the higher ballistic coefficient. The TPS mass required also increased due to the reduced area exposed to the heating environment, leading to a higher total mass for the lower FR. A comparison of these parameters for the 20 mt and 22 mt payload options are shown in Fig. 11. Like the results found in Tables 3-6, 100 % of cases in Table 7 met the 50 m requirement. These results indicate the robustness of the vehicle design and G&C methods employed.

Table 7. FP^{2}DG gain comparison of Monte Carlo 99.75%-tile results at the ground.

Parameter	FR=1.78, 20mt payload, 100 kN thrust **99.75%-tile**	FR=2.25, 20mt payload, 100 kN thrust **99.75%-tile**	FR=2.25, 22mt payload, 100 kN thrust **99.75%-tile**
Peak Heat Rates (W/cm^2)	6.02E+01	5.65E+01	5.77E+01
Peak G-loads (g)	3.78E+00	3.77E+00	3.77E+00
Miss Distance at Ground (m)	7.42E+00	5.72E+00	5.63E+00
Horizontal Velocity at Ground (m/s)	2.00E+00	2.48E+00	2.58E+00
Vertical Velocity at Ground (m/s)	3.83E+00	3.79E+00	3.77E+00
ME Propellant Used at Ground (mt)	1.04E+01	1.11E+01	1.20E+01

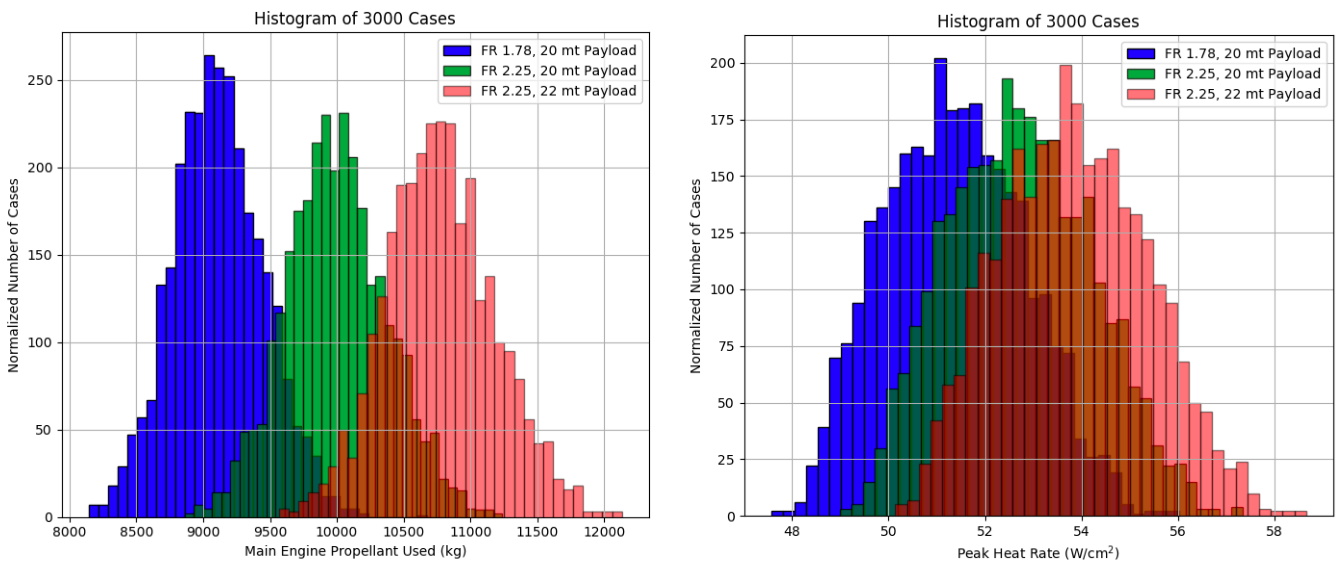

(a) (b)

Fig. 11 Comparison of key performance parameters for vehicle updates (100 kN main engines): a) Main engine propellant usage; b) Peak heat rate.

IV. Conclusion

Trade studies on the effects of updates in main engine modeling, guidance and control, vehicle mass properties, and SRP aerodynamic-propulsive interaction modeling have been presented for a 6-DoF simulation for human Mars EDL. While these updates have the potential to increase the difficulty of achieving the target within the precision landing target radius of 50 m, they provide important steps to increase the fidelity and understanding of the mission as a whole. An upgrade to FP^{2}DG from TAPDG has offered large propellant savings due to the automated PDI prediction logic. To maximize the trajectory shaping benefits of FP^{2}DG, a trade study on different gains was performed for nominal and dispersed cases. The effects aerodynamic-propulsive interaction has been explored using a preliminary model. The mitigation strategy of increasing the distance between the main engines to increase pitch authority was applied and resulted in improved attitude tracking. Lastly, a study in changes to the vehicle due to possible mission concepts of operations updates has been explored. The changes of increasing the payload to 22 mt and decreasing the fineness ratio of the vehicle have not shown significant changes to landing performance in nominal or dispersed cases. It is recommended that FP^{2}DG be used in future studies, as the trajectory shaping feature benefits the integrated GN&C problem. Once a representative aerodynamic-propulsive interaction model is provided, it is recommended that Monte Carlo analysis is used to assess impacts on performance. Other future work includes implementing main engine throttle keep-out zones, improving attitude control in powered descent to decrease final horizontal velocities, and updating entry aerodynamic databases based on results from flap actuator and RCS wind tunnel testing. Future analysis also evaluate the impacts of navigation errors on the full GN&C EDL performance.

V. Acknowledgements

The authors would like to thank Joseph Garcia, Jeffrey Bowles, Phil Robinson, Ashley Korzun, Stan Bouslog, Daniel Matz, Damien Calderon, and Ellen Braden for their invaluable contributions. The authors would also like to thank Alicia Cianciolo and Tara Polsgrove for their leadership and support of this work.

References

[1] Cianciolo, A. D., Polsgrove, T. T. “Human Mars Entry, Descent, and Landing Architecture Study Overview”, SPACE 2016, AIAA 2016-5494.

[2] Lu, P. “Augmented Apollo Powered Descent Guidance”, Journal of Guidance, Control, and Dynamics, Vol. 42, No. 3 (2019), pp. 447-457.

[3] Johnson, B., Lu, P., and Cerimele, C. “Mid-Lift-to-Drag Ratio Rigid Vehicle Performance Using Tunable Apollo Powered Guidance”, AAS 2019, Portland, Maine.

[4] Cianciolo, A.D., Korzun, A., Edquist, K., Samareh, J., Polsgrove, T., Sostaric, T., Calderon, D., Garcia, J. A., “Human Mars Entry, Descent, and Landing Architecture Study: Phase 3 Summary”, AIAA SciTech 2020, Jan. 2020.

[5] Korzun, A., Canabal, F., Tang, C., Childs, R., Van Norman, J., Tynis, J., Bibb, K. “Computational Investigation of Powered Descent for Human-Scale Mars Landers.” AIAA SciTech 2020 Abstract Accepted.

[6] Lu, P., “Theory of Fractional-Polynomial Powered Descent Guidance”, Journal of Guidance, Control, and Dynamics, available online 2019. doi:https://doi.org/10.2514/1.G004556

[7] Lu, P., “Entry Guidance: A Unified Method”, Journal of Guidance, Control, and Dynamics, Vol. 37, No. 3 (2014), pp. 713-728.

[8] Brown, J.L., Garcia, J.A., Kinney, D.J., Bowles, J.V., Mansour, N.N., U.S. Patent entitled “Co-Optimization of Blunt Body Shapes for Moving Vehicles” issued in 2014, Patent No.: US8725470

[9] Garcia, J.A., Brown, J. L., Kinney D. J., Bowles, J. V., Huynh L.C., Jiang X.J., Lau E., Dupzyk, I.C., “Co-Optimization of Mid Lift to Drag Vehicle Concepts for Mars Atmospheric Entry,” 10th AIAA/ASME Thermophysics Conference, 2010.

[10] D’Souza, C., “An Optimal Guidance Law for Planetary Landing”, AIAA-97-3709, 1997.

[11] Lu, P., “Propellant-Optimal Powered Descent Guidance”, Journal of Guidance, Control, and Dynamics, Vol. 41, No. 4, 2018, pp. 813–826. doi:https://doi.org/10.2514/1.G003243 JGCODS 0731-5090

[12] Nichols, R., and Buning, P., User’s Manual for OVERFLOW 2.1t, University of Alabama, Birmingham, AL, Aug. 2008.

[13] Wright, M. W., White, T., and Mangini, N., “Data Parallel Line Relaxation (DPLR) Code User Manual Acadia Version 4.01.1,” NASA TM-2009-215388, Oct. 2009.

[14] McGuire, M. K., Bowles, J., Yang, L., Kinney, D., Roberts, C., “TPS Selection & Sizing Tool Implemented in an Advanced Engineering Environment,” AIAA-2004-342, 42nd AIAA Aerospace Sciences Meeting and Exhibit.

[15] Johnson, B., Cerimele, C., Stachowiak, S., Sostaric, R., Matz, D., Lu, P., “Mid-Lift-to-Drag Ratio Rigid Vehicle Control System and Simulation for Human Mars Entry”, AIAA, SciTech 2018, Kissimmee, Florida.